Thermal interface conductance across metal alloy–dielectric interfaces

Justin P. Freedman,[1] Xiaoxiao Yu,[2] Robert F. Davis,[1] Andrew J. Gellman,[1,2,3] and Jonathan A. Malen[1,4,*]
[1]*Department of Materials Science and Engineering, Carnegie Mellon University, Pittsburgh, Pennsylvania 15213, USA*
[2]*Department of Chemical Engineering, Carnegie Mellon University, Pittsburgh, Pennsylvania 15213, USA*
[3]*Department of Chemistry, Carnegie Mellon University, Pittsburgh, Pennsylvania 15213, USA*
[4]*Department of Mechanical Engineering, Carnegie Mellon University, Pittsburgh, Pennsylvania 15213, USA*
(Received 14 October 2015; revised manuscript received 23 December 2015; published 21 January 2016)

We present measurements of thermal interface conductance as a function of metal alloy composition. Composition spread alloy films of Au_xCu_{1-x} and Au_xPd_{1-x} solid solutions were deposited on single crystal sapphire substrates via dual electron-beam evaporation. High throughput measurements of thermal interface conductance across the (metal alloy)-sapphire interfaces were made by positional scanning of frequency domain thermoreflectance measurements to sample a continuum of Au atomic fractions ($x \sim 0 \rightarrow 1$). At a temperature of 300 K, the thermal interface conductance at the Au_xCu_{1-x}-sapphire interfaces monotonically decreased from $197 \pm 39\,\mathrm{MW\,m^{-2}\,K^{-1}}$ to $74 \pm 11\,\mathrm{MW\,m^{-2}\,K^{-1}}$ for $x = 0 \rightarrow 0.95 \pm 0.02$ and at the Au_xPd_{1-x}-sapphire interfaces from $167 \pm 35\,\mathrm{MW\,m^{-2}\,K^{-1}}$ to $60 \pm 10\,\mathrm{MW\,m^{-2}\,K^{-1}}$ for $x = 0.03 \rightarrow 0.97 \pm 0.02$. To shed light on the phonon physics at the interface, a Diffuse Mismatch Model for thermal interface conductance with alloys is presented and agrees reasonably with the thermal interface conductance data.

DOI: 10.1103/PhysRevB.93.035309

I. INTRODUCTION

Thermal conduction in electronic devices is a function of the thermal conductivity of the device materials and the thermal interface conductance (G) across material interfaces. As material and device length scales become commensurate to energy carrier mean free paths (MFPs), thermal conduction through electronic devices is controlled by G across material interfaces. Many studies have measured and predicted G across a variety of material interfaces, such as transfer printed metal films [1], graphene/graphite-polymer interfaces [2], and self-assembled monolayer junctions [3], but metal-dielectric interfaces are the most common interfacial feature of contemporary electronic and optoelectronic applications. Presently, G across metal-dielectric interfaces has been extensively measured [4–9] and modeled [10–14], but a systematic study of metal alloy composition's influence on G has not been considered.

Understanding the role that metal alloy composition plays on G across a metal-dielectric interface is important because metal alloys provide multifunctional solutions to optimize thermal and nonthermal properties of metal-dielectric interfaces. For example, in heat-assisted magnetic recording (HAMR), a promising next generation data storage technology [15], a gold (Au) near field transducer (NFT) is used to generate plasmons that locally heat regions of the magnetic media [16,17]. Plasmons driven along the Au-dielectric interface generate heat in the Au, which must be dissipated across the interface and into the surrounding dielectric [16]. Low G across the Au-dielectric interface is a major source of thermal resistance within the device and amplifies the temperature rise in the Au NFT, leading to structural and thermal instability [16]. In this and other plasmonic applications, the thermal properties and the plasmonic/optical properties of the metal-dielectric interface must be balanced to optimize performance. For such multifunctional demands, (metal alloy)-dielectric interfaces may be ideal. A secondary reason for studying G across (metal alloy)-dielectric interfaces is that interatomic diffusion across metal-metal interfaces may create unintentional (metal alloy)-dielectric interfaces in devices, e.g., in the case of a miscible adhesion layer [18].

The thermal transport mechanisms that govern the relationship between G and alloy composition are unknown, in contrast to the relationship between thermal conductivity and alloy composition. Thermal conductivity as a function of alloy composition exhibits a characteristic "U-shape" because long energy carrier MFPs are suppressed, even at dilute concentrations, due to impurity scattering. On the other hand, G across metal-dielectric interfaces is not controlled by MFPs, but rather phonon energy transmission at the interface. Measurements of G across (pure metal)-(dielectric alloy) interfaces have exhibited nonmonotonic behavior with alloy composition as a result of nonequilibrium thermal resistance between high frequency phonons that control G and low frequency phonons that carry heat in the dielectric [19]. Furthermore, thermal conductivity measurements of alloy superlattices have shown that alloy composition plays an important role in the acoustic phonon mismatch at the interfaces [20–22]. Therefore, a systematic study of G across (metal alloy)-dielectric interfaces is both technologically and scientifically important.

Here, we report measurements of G across Au_xCu_{1-x}-sapphire and Au_xPd_{1-x}-sapphire interfaces as a function of Au atomic fraction (x). Compositionally graded metal alloy films were deposited on sapphire substrates to enable high throughput measurements of G over a wide range of Au atomic fractions with a single binary alloy sample. A Diffuse Mismatch Model (DMM)-based prediction of phonon thermal conductance as a function of Au atomic fraction is presented and is shown to agree reasonably with the experimental measurements.

*Corresponding author: jonmalen@andrew.cmu.edu

II. EXPERIMENTAL

A. Deposition and characterization of composition spread alloy films

Binary graded alloy films, also known as composition spread alloy films (CSAFs), were deposited onto *c*-plane cut sapphire substrates using a rotatable shadow mask deposition tool equipped with four electron-beam (e-beam) evaporators (Mantis Deposition, Inc.) [23]. The tool is capable of depositing multiple metallic elements simultaneously onto a substrate with each metallic component generated independently by e-beam physical vapor deposition. The shadow masks located between each e-beam source and the substrate determine the location and spatial extent of the metal flux gradient at the substrate position.

In this paper, the dielectric substrates were 14×14 mm^2 [0001]-oriented (*c*-plane cut), polished, single crystal sapphire wafers. Each sapphire substrate was attached to the sample holder by four spring tension screws. The sample holder contained a resistive ceramic heater. A type-*N* thermocouple was spot welded to the backside of the sample holder to monitor the temperature of the sample. The Au, Cu, and Pd pellets were loaded into tungsten crucibles on three e-beam evaporators and then mounted onto the rotating shadow mask CSAF deposition tool. The chamber was sealed and evacuated with a mechanical pump and a turbomolecular pump in sequence to achieve an ultrahigh vacuum. The system was baked for 24 h and subsequently cooled to room temperature. Codeposition of the alloy components was carried out at a pressure of roughly 10^{-9} Torr and a substrate temperature of 300 K. The three e-beam sources containing Au, Cu, and Pd were degassed by gradually increasing the beam power until a constant flux reading was obtained from the ion flux monitor. The deposition rates were calibrated to be 0.2 nm min^{-1} with a Maxtek quartz crystal microbalance positioned at the location of the substrate during deposition. The Cu and Pd flux gradients were orientated at 90° from the Au flux gradient by appropriate orientation of the two shadow masks. After deposition of the CSAFs, the samples were annealed at 800 K for 30 min (chosen based on the Au_xCu_{1-x} [24] and Au_xPd_{1-x} [25] phase diagrams) by conductive heat transfer from the resistively heated sapphire substrate. The annealing ensured that the CSAFs contained face centered cubic crystalline solid solutions, without intermetallics, across all compositions [26]. After cooling, the chamber was vented to remove the sample for composition and thickness vs position analysis.

The local composition and thickness across the CSAFs were determined using energy dispersive x-ray (EDX) spectroscopy conducted in a TESCAN scanning electron microscope with an Oxford Instruments X-Max detector. The EDX measurements were made over a 13×13 grid of points spaced by 1 mm and spanning 12×12 mm^2 in the center of the 14×14 mm^2 deposition substrate. At each point, the EDX signal was collected by rastering the 20 keV beam over a $50 \times 50\,\mu$m^2 area. To account for the sample morphology consisting of a thin homogenous alloy film (<100 nm) on a sapphire substrate, the EDX intensities were analyzed using the ThinFilmID software to yield composition and thickness [27]. The uncertainties in the reported thicknesses as a function of sample position are ±5% of the nominal values. Figures 1(a) and 1(b) show the

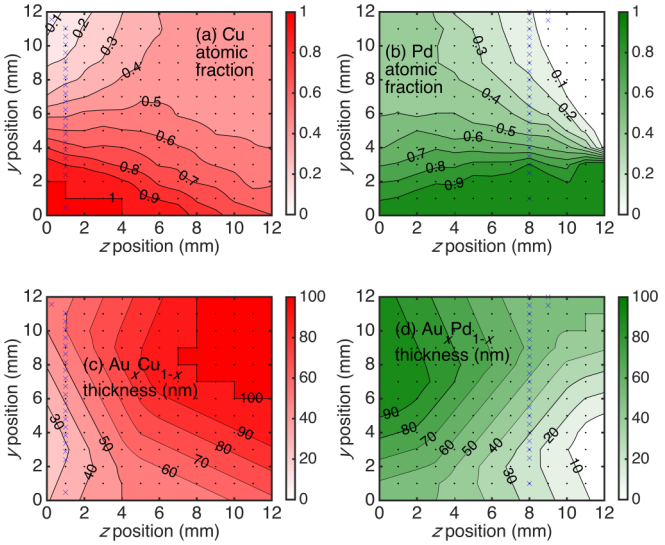

FIG. 1. (a) Cu and (b) Pd atomic fraction of the Au_xCu_{1-x} and Au_xPd_{1-x} CSAFs as a function of the z and y coordinates on the sapphire substrate surface. (c) Au_xCu_{1-x} and (d) Au_xPd_{1-x} film thickness as a function of the z and y coordinates on the sapphire substrate surface. The black dots indicate EDX measurement positions and the blue crosses designate the measured positions of G on the samples.

Cu and Pd composition in atomic fraction, while Figures 1(c) and 1(d) show the CSAF thickness as a function of position on the sapphire substrate for the Au_xCu_{1-x} [Figs. 1(a) and 1(c)] and Au_xPd_{1-x} films [Figs. 1(b) and 1(d)]. The black dots in Fig. 1 indicate the EDX measurements positions and the blue crosses represent the measured positions of G on the samples.

B. High throughput frequency domain thermoreflectance measurements

To measure G across the metal alloys and the sapphire substrate, as a function of metal alloy composition, the samples were attached to a micromanipulator for submicron precision control of sample position. Similar to high throughput thermoreflectance measurements of Ni alloy thermal conductivity by Zheng *et al.* [28], frequency domain thermoreflectance (FDTR) [29–31] was used to measure G at various positions on the 12×12 mm^2 compositionally mapped region of the samples. FDTR is a noncontact optical pump-probe technique used to measure thermal transport. An electro-optic modulator intensity modulates a 488 nm wavelength continuous wave (cw) pump laser beam, which is focused onto the sample inducing a periodic heat flux at the surface. A coaligned cw 532 nm wavelength probe laser beam measures the change in temperature at the sample surface induced by the pump laser, which depends on G across the (metal alloy)-sapphire interface. The phase-lag between the pump and probe beams after they reflect from the sample surface is measured as a function of the pump beam's frequency (100 kHz to ~5 MHz) using a lock-in amplifier. The phase-lag between the reflected pump and probe beams represents the phase difference between the temperature rise and heat flux at the

sample surface. G is determined by fitting the measured phase-lag data to the heat diffusion equation in a layered medium [32], where the only unknown parameter is G for the interface between the metal alloy and sapphire. After a measurement of G was made via FDTR at a given position on the sample, the micromanipulator was used to translate the sample in 480 μm (Au_xCu_{1-x} sample)/500 μm (Au_xPd_{1-x} sample) steps so that the coaligned pump and probe laser beams could measure G at different alloy compositions. The measured locations on the samples were selected based on the thickness of the CSAFs. Thinner regions were chosen to ensure that the FDTR measurement was more sensitive to G than the intrinsic thermal conductance of the CSAF itself (see the Supplemental Material for justification [33]).

The laser spot size diameter was 5.8 ± 0.3 μm, which was significantly smaller than the sample size (12 mm) and the distance between measurements (480/500 μm). Therefore, the local alloy properties of the CSAFs, volumetric heat capacity and thermal conductivity, were assumed to be constant within the individual FDTR-measured regions. The following relationship was used to determine the volumetric heat capacity as a function of the Au atomic fraction [34],

$$C_{\mathrm{Au}_x m_{1-x}}(x) = 3k_B \eta_{\mathrm{Au}_x m_{1-x}} = \frac{12k_B}{(a_{\mathrm{Au}}x + a_m(1-x))^3}, \quad (1)$$

where $C_{\mathrm{Au}_x m_{1-x}}$ is the volumetric heat capacity of the metal alloy, m represents Cu or Pd, k_B is the Boltzmann constant, a is the lattice constant of Au, Cu, or Pd, and $\eta_{\mathrm{Au}_x m_{1-x}}(x) = \frac{4}{(a_{\mathrm{Au}}x + a_m(1-x))^3}$ is the primitive cell number density for the face centered cubic crystal alloys. Equation (1) assumes that the high temperature approximation is valid for Au, Pd, and Cu at 300 K (Debye temperatures are 170 K [34], 275 K [35], and 344 K [34], respectively) and uses Vegard's law to describe the lattice parameter of the alloys. Under these assumptions, the elemental volumetric heat capacities, C_{Au}, C_{Cu}, and C_{Pd}, were within 2% of the literature values [36,37]. The thermal conductivity of sapphire was assumed to be 38 ± 2 W m^{-1} K^{-1}, based on prior measurements [38]. Nondiffusive thermal transport in the sapphire substrate was not present for the laser spot size and range of heating frequencies used in this paper because 95% of sapphire's thermal conductivity results from phonons with MFPs less than 1 μm [39]. The bulk values of metallic alloy thermal conductivity found in Ref. [40] (plotted in the Supplemental Material [33]) were chosen as the thermal conductivity of the metal alloys because the electron MFP in the metal alloys is on the order of nanometers (calculated using $l_e = \frac{3\Lambda_{\mathrm{bulk}}}{C_e v_e}$, where l_e is the electron MFP, Λ_{bulk} is the bulk metal alloy thermal conductivity, C_e is the volumetric heat capacity of the electrons, and v_e is the electron velocity), while the film thickness of the measured regions of the metal alloys was between 24 and 60 nm. Since the measured G is not highly sensitive to the thermal conductivity of the metal alloys, a bulk value of thermal conductivity in the metal alloys was a reasonable choice to model the measured data (values of thermal conductivity were varied between the bulk value and 50% of the bulk value to establish the uncertainty due to this assumption; see the Supplemental Material [33]). A Au transducer film of 55 ± 0.3 nm was sputtered on top of the Au_xPd_{1-x} sample at a temperature of 300 K (with no expectation of diffusion into the CSAF) via a Perkin Elmer 6J Sputtering System to enhance the thermoreflectance signal. A Au transducer film was not required to achieve an adequate thermoreflectance signal with the Au_xCu_{1-x} CSAF. The thickness of the Au transducer layer was measured by x-ray reflectivity, and its thermal conductivity was measured to be 130 ± 6 W m^{-1} K^{-1} using a four-point electrical conductivity measurement and the Wiedemann-Franz law.

III. RESULTS AND DISCUSSION

The measured values of G as a function of Au atomic fraction for Au_xCu_{1-x}-sapphire and Au_xPd_{1-x}-sapphire interfaces at a temperature of 300 K are shown in Fig. 2. Both interfaces exhibit monotonically decreasing G as a function of increasing Au atomic fraction in the metal alloys. On the left side of Fig. 2, where nearly (pure Pd)-sapphire and (pure Cu)–sapphire interfaces were measured, the Cu-sapphire interface (197 ± 39 MW m^{-2} K^{-1}) exhibits a greater G than that of the Pd-sapphire interface (167 ± 35 MW m^{-2} K^{-1}), though uncertainty weakens this distinction. The G across the Au_xCu_{1-x}–sapphire interface was measured to be 74 ± 11 MW m^{-2} K^{-1} at $x = 0.95 \pm 0.02$, and the G across the Au_xPd_{1-x}–sapphire interface was measured to be 60 ± 10 MW m^{-2} K^{-1} at $x = 0.97 \pm 0.02$, matching previous measurements of a Au-sapphire interface [5]. The inset in Fig. 2 shows FDTR phase-lag data as a function of the heating frequency for three Au atomic fractions in the Au_xPd_{1-x}–sapphire sample and fits to the heat diffusion equation used to extract G [32]. The distinct phase values for otherwise identical samples enables clear resolution of G across all Au fractions. The uncertainty in the measured G, presented in Fig. 2, is due to the uncertainty

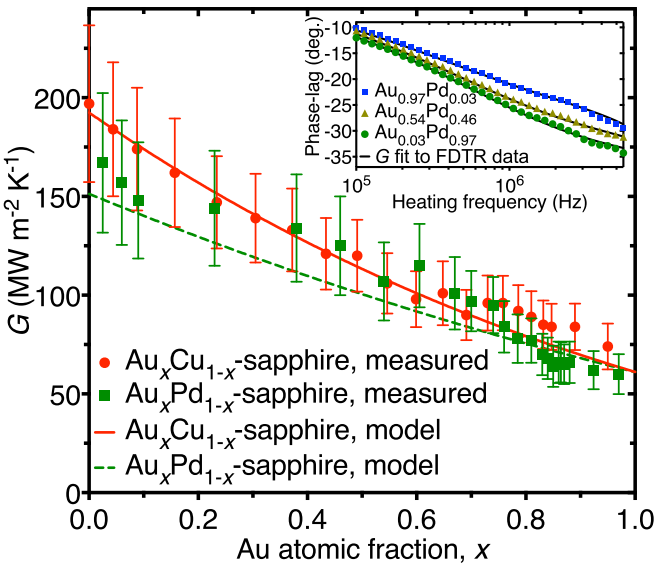

FIG. 2. Measured values of G and DMM-based predictions of G_p across Au_xCu_{1-x}-sapphire and Au_xPd_{1-x}-sapphire interfaces as a function of Au atomic fraction, x. The inset at the top right shows FDTR phase-lag vs heating frequency data with fits to the heat diffusion equation used to extract G for three Au atomic fractions in the Au_xPd_{1-x}-sapphire sample.

from the (i) laser beam spot size (±5%), (ii) sapphire thermal conductivity (±2 $W\,m^{-1}\,K^{-1}$), (iii) thickness of the metal alloy layer (±5%), (iv) heat capacity of the metal alloy layer (±5%), and (v) metal alloy thermal conductivity (uncertainty ranges from the bulk value to 50% of the bulk value). To determine the size of the error bars, the FDTR-measured phase-lag vs heating frequency data was fit to the heat diffusion equation to extract the deviations in G when (i) through (v) were independently varied within their respective uncertainties [30]. The total uncertainty results from the square root of the sum of the squares of these independent deviations in G. The uncertainty in G due to the uncertainty in (i) through (v) is presented in the Supplemental Material [33].

At a metal-dielectric interface, electrons that carry heat within the metal transfer it to phonons that transmit the energy across the interface in a process known as electron-phonon coupling [41]. Electron-phonon coupling has been modeled as a thermal resistance process that is in series with the phonon energy transmission across the interface [42–44]. The values of G reported in Fig. 2 represent the composite G due to the electron-phonon coupling conductance ($G_{e\text{-}p}$) and the phonon transmission conductance (G_p). We have chosen to report the composite value because the influence of metal alloy composition on the electron-phonon coupling coefficient is unknown in Au_xCu_{1-x} and Au_xPd_{1-x} thin films. Based on the paper by Majumdar and Reddy [41] and the bulk properties of Au [45,46], Cu [47,48], and Pd [49] (the electron-phonon coupling coefficient was determined based on the equation in Table 1 in Ref. [50], where the Debye temperature, electronic heat capacity parameter, and McMillan factor were found in Refs. [35,51,52], respectively), we estimate that $G_{e\text{-}p}$ is ~300 $MW\,m^{-2}\,K^{-1}$ in Au, ~700 $MW\,m^{-2}\,K^{-1}$ in Cu, and ~2 $GW\,m^{-2}\,K^{-1}$ in Pd. The values of $G_{e\text{-}p}$ are many times greater than the measured values of G in Fig. 2, indicating that the FDTR measurement is primarily sensitive to G_p.

To model the metal-dielectric interface, we neglect electron-phonon coupling and compare the data to predictions of G_p. Therefore, Eq. (2) neglects electron-phonon coupling and assumes diffuse scattering at the interface, quasiequilibrium phonon transport across the interface, and isotropic phonon dispersion [10],

$$G_p = \frac{1}{8\pi^2}\sum_j \int_{\omega_{j,\text{metal}}} \hbar\omega_{j,\text{metal}} k^2{}_{j,\text{metal}}\,\alpha \frac{\partial n}{\partial T} d\omega_{j,\text{metal}}, \quad (2)$$

where $\hbar$ is the reduced Planck constant, ω is phonon frequency, k is phonon wave vector, α is the phonon frequency-dependent energy transmission coefficient from the metal to the dielectric, n is the Bose-Einstein distribution, T is temperature, and j represents polarization. The DMM predicts α by comparing the relative phonon density of states for the two materials at a given phonon frequency under the assumption of elastic scattering at the metal-dielectric interface [10], where

$$\alpha(\omega) = \frac{\sum_j [k_{j,\text{sapphire}}(\omega)]^2}{\sum_j [k_{j,\text{sapphire}}(\omega)]^2 + \sum_j [k_{j,\text{metal}}(\omega)]^2}. \quad (3)$$

Equation (3) represents the probability that a phonon of frequency ω in the metal will transport energy across the metal-dielectric interface into the sapphire.

To understand the behavior of G_p as a function of metal alloy composition, a DMM-based prediction using real phonon dispersion for the sapphire substrate and Born–von Karman (BvK) [11,53,54] phonon dispersion for the metal alloy films was developed. To approximate real phonon dispersion for [0001] sapphire [55], the longitudinal and transverse acoustic phonon branches were fit to a fourth order polynomial, $\omega_{\text{sapphire}}(k) = Ak^4 + Bk^3 + Ck^2 + Dk$ [10], where A, B, C, and D are polynomial coefficients. The BvK dispersion relationship was used for the metal alloys because it allows for simple mixing rules to be applied, such that G_p can be determined continuously across all atomic alloy fractions. The BvK dispersion is also more accurate than Debye dispersion because it accounts for the reduced group velocity near the Brillouin zone edge [54]. As a first approximation, we linearly interpolated the sound velocity at the Brillouin zone center and used Vegard's law to determine the lattice parameter of the alloys. The mixing rules used for the alloys were

$$a_{\text{Au}_x m_{1-x}}(x) = a_{\text{Au}}x + a_m(1-x), \quad (4)$$

$$v_{L,\text{Au}_x m_{1-x}}(x) = v_{L,\text{Au}}x + v_{L,m}(1-x), \quad (5)$$

$$v_{Tr,\text{Au}_x m_{1-x}}(x) = v_{Tr,\text{Au}}x + v_{Tr,m}(1-x), \quad (6)$$

where v is the sound velocity of the acoustic phonon branches of the metals, L represents the longitudinal acoustic phonon branch of the metals, and Tr represents the transverse acoustic phonon branch of the metals. Using Eqs. (4)–(6), the smallest allowed wavelength $\lambda_{\text{Au}_x m_{1-x}}$ and the acoustic phonon frequencies at the [111] Brillouin zone edge $\omega_{0,\text{Au}_x m_{1-x}}$ are defined for the metal alloys as [54]

$$\lambda_{\text{Au}_x m_{1-x}} = \frac{2\pi}{(6\pi^2\eta_{\text{Au}_x m_{1-x}})^{1/3}}, \quad (7)$$

$$\omega_{0,L,\text{Au}_x m_{1-x}} = \frac{2\sqrt{3}v_{L,\text{Au}_x m_{1-x}}}{\lambda_{\text{Au}_x m_{1-x}}}, \quad (8)$$

$$\omega_{0,Tr,\text{Au}_x m_{1-x}} = \frac{2\sqrt{3}v_{Tr,\text{Au}_x m_{1-x}}}{\lambda_{\text{Au}_x m_{1-x}}}. \quad (9)$$

Combining Eqs. (7)–(9), the BvK phonon dispersion relationships for the longitudinal and transverse branches of the metal alloys are

$$\omega_{L,\text{Au}_x m_{1-x}}(k) = \omega_{0,L,\text{Au}_x m_{1-x}} \sin\left(\frac{\lambda_{\text{Au}_x m_{1-x}} k}{2\sqrt{3}}\right), \quad (10)$$

$$\omega_{Tr,\text{Au}_x m_{1-x}}(k) = \omega_{0,Tr,\text{Au}_x m_{1-x}} \sin\left(\frac{\lambda_{\text{Au}_x m_{1-x}} k}{2\sqrt{3}}\right). \quad (11)$$

Figure 3 shows the real and BvK phonon dispersion relations for Au [56] [Fig. 3(a)], Cu [57] [Fig. 3(b)], and Pd [58] [Fig. 3(c)] in the [111] direction, the real phonon dispersion and the accompanying fourth order polynomial fit for sapphire [55] in the [0001] direction, and the transmission coefficient for Au-sapphire [Fig. 3(a)], Cu-sapphire [Fig. 3(b)], and Pd-sapphire [Fig. 3(c)] interfaces as a function of phonon frequency using BvK dispersion in the metals. Although thermal interface conductance across aluminum-sapphire interfaces has been shown to depend on the sapphire's orientation [59], isotropic phonon dispersion, based on the [0001] and [111] directions for the sapphire and the metals, respectively, was chosen to approximate phonon dispersion in all directions.

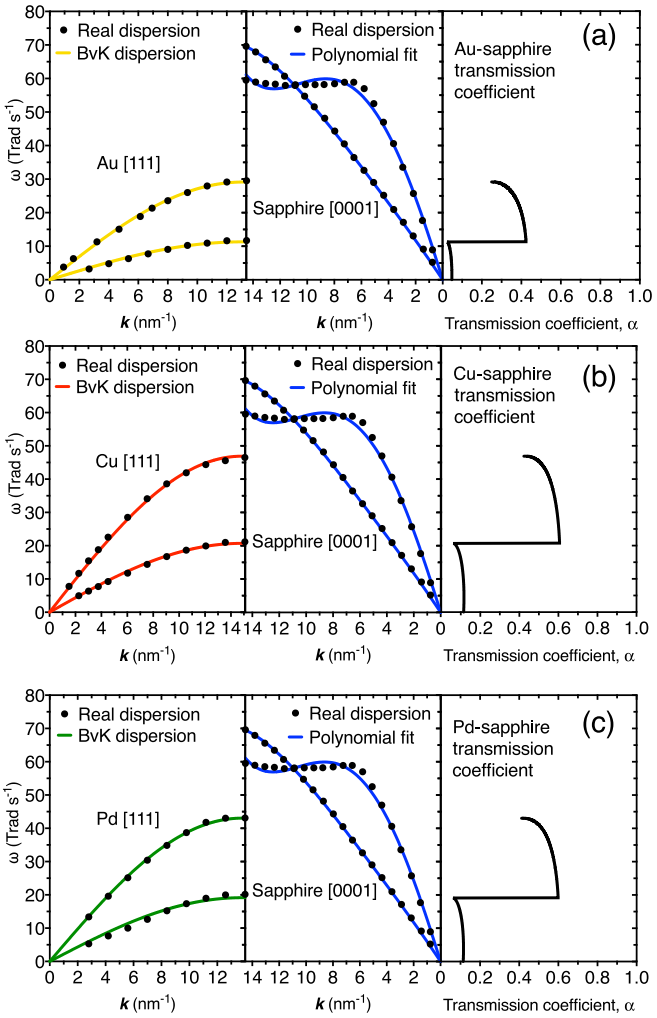

FIG. 3. In the left column are BvK approximations to the real phonon dispersion for (a) Au, (b) Cu, and (c) Pd in the [111] direction. In the middle column are fourth order polynomial fits to the real dispersion for sapphire in the [0001] direction. In the right column are the phonon frequency-dependent energy transmission coefficients, $\alpha(\omega)$, for phonons transporting from the metal into the sapphire for (a) the Au-sapphire interface, (b) the Cu-sapphire interface, and (c) the Pd-sapphire interface based on BvK dispersion in the metal and the polynomial fit to the real dispersion in sapphire.

The [111] direction was chosen for Au [60], Cu [60,61], and Pd [62] because these metals have been shown to preferentially grow along the [111] direction on c-plane sapphire. Sound velocities of $v_{L,\mathrm{Au}} = 3485\,\mathrm{m\,s^{-1}}$, $v_{Tr,\mathrm{Au}} = 1352\,\mathrm{m\,s^{-1}}$, $v_{L,\mathrm{Cu}} = 4963\,\mathrm{m\,s^{-1}}$, $v_{Tr,\mathrm{Cu}} = 2191\,\mathrm{m\,s^{-1}}$, $v_{L,\mathrm{Pd}} = 4910\,\mathrm{m\,s^{-1}}$, and $v_{Tr,\mathrm{Pd}} = 2184\,\mathrm{m\,s^{-1}}$ were used for the longitudinal and transverse acoustic branches of Au, Cu, and Pd, respectively. The values of sound velocity were determined by fitting the BvK dispersion to the real dispersion data, based on neutron scattering, with a nonlinear regression method.

The transmission coefficients of Au, Cu, and Pd exhibit a discontinuity as a function of phonon frequency in Fig. 3. Phonons with frequencies less than the maximum frequency in the transverse branch of the metals have a greater chance of being reflected than phonons with higher frequencies because both transverse and longitudinal modes are available for reflection. Higher frequency phonons in the metal can only reflect into longitudinal acoustic modes at the interface. Therefore, the phonon frequencies greater than the maximum frequency in the metals' transverse branch have a much greater probability of transmission across the metal-sapphire interface causing $\alpha(\omega)$ to exhibit a discontinuity. Notably, if mode conversion between longitudinal and transverse phonons was disallowed, the transmission coefficients would monotonically decrease with phonon frequency without a discontinuity.

The monotonic behavior of G_p as a function of metal alloy composition in Fig. 2 can be explained by an examination of Fig. 3. Phonon frequencies in Au are less than those in Pd and Cu, as shown on the left side of Fig. 3. These relatively higher frequency phonons in Pd and Cu elastically scatter with modes in sapphire that have a high density of states, resulting in high $\alpha(\omega)$ from the metal to the sapphire. These high frequency phonons dominate G_p across the metal-sapphire interface. As the Au atomic fraction increases, the phonon frequencies decrease causing G_p to monotonically decrease.

Although the experimental G data agrees reasonably with the DMM-based prediction of G_p, it should be noted that the DMM has limitations. For example, it is not rigorous to determine the probability of phonon energy transmission across material boundaries based only on the overlap in the phonon density of states without considering the interface details. The DMM is a simple predictive tool that provides approximate values of G_p, but can deviate significantly from experimental data, depending on the materials [5,43].

The trend in G_p can be analytically demonstrated by integrating Eq. (2) under the high temperature approximation ($\frac{\partial n}{\partial T} = \frac{k_B}{\hbar\omega}$), assuming triply degenerate Debye dispersion in the metal and sapphire. In this case, the expression for G_p becomes

$$G^{\mathrm{Debye}}_{p,\mathrm{Au}_x m_{1-x}}(x) = \frac{3k_B \eta_{\mathrm{Au}_x m_{1-x}} v_{\mathrm{Au}_x m_{1-x}}}{4\left(1+\frac{v^2_{\mathrm{sapphire}}}{v^2_{\mathrm{Au}_x m_{1-x}}}\right)} = \frac{C_{\mathrm{Au}_x m_{1-x}} v_{\mathrm{Au}_x m_{1-x}}}{4\left(1+\frac{v^2_{\mathrm{sapphire}}}{v^2_{\mathrm{Au}_x m_{1-x}}}\right)}. \tag{12}$$

Since Cu has the largest sound velocity and volumetric heat capacity, it exhibits the largest G_p with sapphire, followed by Pd and Au. As x increases, both $C_{\mathrm{Au}_x m_{1-x}}$ and $v_{\mathrm{Au}_x m_{1-x}}$ decrease, causing $G^{\mathrm{Debye}}_{p,\mathrm{Au}_x m_{1-x}}$ to decrease, as predicted for G_p with more accurate dispersion.

IV. CONCLUSION

This article presents measurements of the influence of solid solution metal alloy composition on G across metal-dielectric interfaces. $\mathrm{Au}_x\mathrm{Cu}_{1-x}$ and $\mathrm{Au}_x\mathrm{Pd}_{1-x}$ CSAFs were deposited on sapphire substrates to enable high throughput measurements of G as a function of metal alloy composition via FDTR and agreed favorably with DMM-based predictions. For multifunctional interfaces, where thermal reliability is a concern, metal alloys offer unique control for optimization of thermal and nonthermal properties. This paper opens new avenues for addressing exciting questions with regard to

(metal alloy)–dielectric interfaces. For example, how do more complex binary and ternary alloys affect G? Can greater G than either (pure metal)-dielectric interface be achieved by control of alloy composition? Further examination of (metal alloy)-dielectric interfaces will provide superior understanding and control of G that is extremely valuable to nascent electronic and optoelectronic applications.

ACKNOWLEDGMENTS

All authors are thankful for financial support from the National Science Foundation, Awards No. CBET-1403447 and No. CBET-0923083, and J. P. Freedman thanks the Natural Sciences and Engineering Research Council of Canada for his doctoral postgraduate scholarship. We thank J. C. Duda (Seagate Technology) for helpful discussions.

[1] D. W. Oh, S. Kim, J. A. Rogers, D. G. Cahill, and S. Sinha, Adv. Mater. **23**, 5027 (2011).
[2] T. F. Luo and J. R. Lloyd, Adv. Funct. Mater. **22**, 2495 (2012).
[3] Z. Wang, J. A. Carter, A. Lagutchev, Y. K. Koh, N. H. Seong, D. G. Cahill, and D. D. Dlott, Science **317**, 787 (2007).
[4] R. J. Stevens, A. N. Smith, and P. M. Norris, J. Heat Transf. **127**, 315 (2005).
[5] R. J. Stoner and H. J. Maris, Phys. Rev. B **48**, 16373 (1993).
[6] E. T. Swartz and R. O. Pohl, Appl. Phys. Lett. **51**, 2200 (1987).
[7] G. T. Hohensee, R. B. Wilson, and D. G. Cahill, Nat. Commun. **6**, 6578 (2015).
[8] H. K. Lyeo and D. G. Cahill, Phys. Rev. B **73**, 144301 (2006).
[9] P. E. Hopkins, P. M. Norris, R. J. Stevens, T. E. Beechem, and S. Graham, J. Heat Transf. **130**, 062402 (2008).
[10] J. C. Duda, T. E. Beechem, J. L. Smoyer, P. M. Norris, and P. E. Hopkins, J. Appl. Phys. **108**, 073515 (2010).
[11] P. Reddy, K. Castelino, and A. Majumdar, Appl. Phys. Lett. **87**, 211908 (2005).
[12] T. Beechem, S. Graham, P. Hopkins, and P. Norris, Appl. Phys. Lett. **90**, 054104 (2007).
[13] T. Beechem and P. E. Hopkins, J. Appl. Phys. **106**, 124301 (2009).
[14] R. Cheaito, J. T. Gaskins, M. E. Caplan, B. F. Donovan, B. M. Foley, A. Giri, J. C. Duda, C. J. Szwejkowski, C. Constantin, H. J. Brown-Shaklee, J. F. Ihlefeld, and P. E. Hopkins, Phys. Rev. B **91**, 035432 (2015).
[15] R. Ikkawi, N. Amos, A. Lavrenov, A. Krichevsky, D. Teweldebrhan, S. Ghosh, A. A. Balandin, D. Litvinov, and S. Khizroev, J. Nanoelectron. Optoelectron. **3**, 44 (2008).
[16] W. A. Challener, C. Peng, A. V. Itagi, D. Karns, W. Peng, Y. Peng, X. Yang, X. Zhu, N. J. Gokemeijer, Y. T. Hsia, G. Ju, R. E. Rottmayer, M. A. Seigler, and E. C. Gage, Nat. Photonics **3**, 220 (2009).
[17] L. Huang, B. Stipe, M. Staffaroni, J. Y. Juang, T. Hirano, E. Schreck, and F. Y. Huang, IEEE Trans. Magn. **49**, 2565 (2013).
[18] M. Jeong, J. P. Freedman, H. J. Liang, C.-M. Chow, V. M. Sokalski, J. A. Bain, and J. A. Malen, Phys. Rev. Appl. (to be published).
[19] R. B. Wilson and D. G. Cahill, Nat. Commun. **5**, 5075 (2014).
[20] S. T. Huxtable, A. R. Abramson, C. L. Tien, A. Majumdar, C. LaBounty, X. Fan, G. Zeng, J. E. Bowers, A. Shakouri, and E. T. Croke, Appl. Phys. Lett. **80**, 1737 (2002).
[21] J. Garg and G. Chen, Phys. Rev. B **87**, 140302 (2013).
[22] C. Dames and G. Chen, J. Appl. Phys. **95**, 682 (2004).
[23] B. Fleutot, J. B. Miller, and A. J. Gellman, J. Vac. Sci. Technol. A **30**, 061511 (2012).
[24] H. Okamoto, D. J. Chakrabarti, D. E. Laughlin, and T. B. Massalski, Bull. Alloy Phase Diagr. **8**, 454 (1987).
[25] H. Okamoto and T. B. Massalski, Bull. Alloy Phase Diagr. **6**, 229 (1985).
[26] D. Priyadarshini, P. Kondratyuk, Y. N. Picard, B. D. Morreale, A. J. Gellman, and J. B. Miller, J. Phys. Chem. C **115**, 10155 (2011).
[27] P. J. Statham, IOP Conf. Ser. Mater. Sci. Eng. **7**, 012027 (2010).
[28] X. Zheng, D. G. Cahill, P. Krasnochtchekov, R. S. Averback, and J. C. Zhao, Acta. Mater. **55**, 5177 (2007).
[29] A. J. Schmidt, R. Cheaito, and M. Chiesa, Rev. Sci. Instrum. **80**, 094901 (2009).
[30] J. A. Malen, K. Baheti, T. Tong, Y. Zhao, J. A. Hudgings, and A. Majumdar, J. Heat Transf. **133**, 081601 (2011).
[31] K. T. Regner, S. Majumdar, and J. A. Malen, Rev. Sci. Instrum. **84**, 064901 (2013).
[32] D. G. Cahill, Rev. Sci. Instrum. **75**, 5119 (2004).
[33] See Supplemental Material at http://link.aps.org/supplemental/10.1103/PhysRevB.93.035309 for justification of $R_{\text{film}} \ll R_{\text{interface}}$, bulk thermal conductivity values of Au_xCu_{1-x} and Au_xPd_{1-x} alloys, and the uncertainty in G due to uncertainty in the laser beam spot size, sapphire thermal conductivity, metal alloy thermal conductivity, metal alloy heat capacity, and metal alloy thickness.
[34] C. Kittel, *Introduction to Solid State Physics* (Wiley, New York, NY, 1996).
[35] J. A. Rayne, Phys. Rev. **118**, 1545 (1960).
[36] G. T. Furukawa, W. G. Saba, and M. L. Reilly, *Critical Analysis of the Heat Capacity Data of the Literature and Evaluation of Thermodynamic Properties of Copper, Silver, and Gold from 0 to 300 K* (National Bureau of Standards, Washington, DC, 1968).
[37] G. T. Furukawa, M. L. Reilly, and J. S. Gallagher, J. Phys. Chem. Ref. Data **3**, 163 (1974).
[38] K. C. Collins, A. A. Maznev, J. Cuffe, K. A. Nelson, and G. Chen, Rev. Sci. Instrum. **85**, 124903 (2014).
[39] Y. Hu, L. Zeng, A. J. Minnich, M. S. Dresselhaus, and G. Chen, Nat. Nanotechnol. **10**, 701 (2015).
[40] C. Y. Ho, M. W. Ackerman, K. Y. Wu, S. G. Oh, and T. N. Havill, J. Phys. Chem. Ref. Data **7**, 959 (1978).
[41] A. Majumdar, and P. Reddy, Appl. Phys. Lett. **84**, 4768 (2004).
[42] A. Giri, J. T. Gaskins, B. F. Donovan, C. Szwejkowski, R. J. Warzoha, M. A. Rodriguez, J. Ihlefeld, and P. E. Hopkins, J. Appl. Phys. **117**, 105105 (2015).
[43] E. T. Swartz and R. O. Pohl, Rev. Mod. Phys. **61**, 605 (1989).
[44] P. Singh, M. Seong, and S. Sinha, Appl. Phys. Lett. **102**, 181906 (2013).
[45] J. G. Cook and M. P. van der Meer, Can. J. Phys. **48**, 254 (1970).

[46] W. Wang and D. G. Cahill, Phys. Rev. Lett. **109**, 175503 (2012).
[47] R. E. B. Makinson, Proc. Phys. Soc. London, Sect. A **67**, 290 (1954).
[48] H. E. Elsayedali, T. B. Norris, M. A. Pessot, and G. A. Mourou, Phys. Rev. Lett. **58**, 1212 (1987).
[49] M. W. Ackerman, K. Y. Wu, and C. Y. Ho, in *Thermal Conductivity 14*, edited by P. G. Klemens and T. K. Chu (Springer Science and Business Media, New York, NY, 1976), pp. 245–257.
[50] J. Hohlfeld, S. S. Wellershoff, J. Gudde, U. Conrad, V. Jahnke, and E. Matthias, Chem. Phys. **251**, 237 (2000).
[51] J. A. Rayne, Phys. Rev. **107**, 669 (1957).
[52] T. Jarlborg, Physica C **385**, 513 (2003).
[53] F. Yang and C. Dames, Phys. Rev. B **87**, 035437 (2013).
[54] C. Dames and G. Chen, in *Thermoelectrics Handbook: Macro to Nano*, edited by D. M. Rowe (CRC Press, Boca Raton, FL, 2006), pp. 42.1–42.16.
[55] H. Schober, D. Strauch, and B. Dorner, Z. Phys. B Condens. Matter **92**, 273 (1993).
[56] J. W. Lynn, H. G. Smith, and R. M. Nicklow, Phys. Rev. B **8**, 3493 (1973).
[57] E. C. Svensson, B. N. Brockhouse, and J. M. Rowe, Phys. Rev. **155**, 619 (1967).
[58] A. P. Miller and B. N. Brockhouse, Can. J. Phys. **49**, 704 (1971).
[59] P. E. Hopkins, T. Beechem, J. C. Duda, K. Hattar, J. F. Ihlefeld, M. A. Rodriguez, and E. S. Piekos, Phys. Rev. B **84**, 125408 (2011).
[60] H. Bialas and K. Heneka, Vacuum **45**, 79 (1994).
[61] T. Sasaki, T. Mizoguchi, K. Matsunaga, S. Tanaka, T. Yamamoto, M. Kohyama, and Y. Ikuhara, Appl. Surf. Sci. **241**, 87 (2005).
[62] C. Muller, H. Muhlbauer, and G. Dumpich, Thin Solid Films **310**, 81 (1997).